Jiao, R., Herman, F., Beyssac, O., Adatte, T., Cox, S. C., Nelson, F. E., Neil, H. L. (2018): Erosion of the Southern Alps of New Zealand during the last deglaciation. - *Geology*, *46*, 11, pp. 975—978.

DOI: http://doi.org/10.1130/G45160.1

Erosion of the Southern Alps of New Zealand during the last deglaciation

Ruohong Jiao[1,2,3], Frédéric Herman[1], Olivier Beyssac[4], Thierry Adatte[5], Simon C. Cox[6], Faye E. Nelson[7], and Helen L. Neil[8]

[1]*Institute of Earth Surface Dynamics, University of Lausanne, 1015 Lausanne, Switzerland*

[2]*Department of Geological and Environmental Sciences, Ben-Gurion University of the Negev, Beer-Sheva 8410501, Israel*

[3]*Helmholtz Centre Potsdam, GFZ German Research Centre for Geosciences, Telegrafenberg, 14473 Potsdam, Germany*

[4]*Institut de Minéralogie, de Physique des Matériaux, et de Cosmochimie, UMR CNRS 7590, Sorbonne Universités - Université Pierre et Marie Curie, 75005 Paris, France*

[5]*Institute of Earth Sciences, University of Lausanne, 1015 Lausanne, Switzerland*

[6]*GNS Science, Private Bag 1930, Dunedin 9054, New Zealand*

[7]*Department of Marine Science, University of Otago, PO Box 56, Dunedin 9054, New Zealand*

[8]*National Institute of Water and Atmospheric Research, Private Bag 14901, Wellington 6021, New Zealand*

ABSTRACT

During the Quaternary, periodic glaciations transformed mountain landscapes. However, how mountain erosion changes between glacier- and river-dominated conditions has been elusive. Here, using samples from an offshore sedimentary core, we estimate the spatial distribution of erosion in the southern part of the Southern Alps of New Zealand during a full transition from the Last Glacial Maximum (LGM), ~20 ka, to the last millennium. Raman spectroscopy analyses of carbonaceous material reveal a marked change in the sediment provenance, which we interpret to reflect the evolving erosion pattern of the mountain range. Over the Holocene since at least ~9 ka, erosion was focused on the chlorite zone schist within the upper reaches of the valleys (>15–20 km distance from the mountain front), possibly dominated by large-magnitude landslides. During the last glaciation, the proportion of sediments from the biotite schist and higher-grade metamorphic rocks in the lower lying areas closer to the mountain front (<15–20 km) was relatively higher, probably the products of glacier carving. Our results suggest that glacier retreat during the last deglaciation caused an upstream localization of the high erosion rates, which is consistent with the snowline records in the Southern Alps and the regional and global climate histories.

INTRODUCTION

The topography of a tectonically active mountain range is heavily influenced by surface processes, such as fluvial, glacial and hillslope erosion, which are strongly controlled by climate. Although it remains a subject of debate (e.g., Herman and Champagnac, 2016; Willenbring and Jerolmack, 2016), climate cooling has been proposed to have increased mountain erosion rates since the Plio-Pleistocene (Herman et al., 2013; Zhang et al., 2001). Accelerated erosion can be explained by expansion of alpine glaciers, which have been found to be locally more erosive than rivers (Hallet et al., 1996). However, other field observations suggest that fluvial incision and hillslope erosion can be as efficient as glacial erosion in tectonically active regions (e.g., Burbank et al., 1996; Koppes and Montgomery, 2009; Larsen and Montgomery, 2012). The apparent conundrum in part reflects the lack of constraints on how erosion rates are distributed in space and time, especially during climatic transitions.

Sediment fluxes measured at outlets of modern rivers and glaciers have been used to estimate catchment-averaged erosion at seasonal to decadal scales (e.g., Dadson et al., 2003; Koppes et al., 2015), but they provide little constraints on how erosion varies spatially within a catchment. Here, based on a semiquantitative provenance analysis of sediments from an offshore core, we are able to estimate the spatial distribution of the relative erosion intensity at catchment scale as well as the variation of this distribution through time. Our approach is based on Raman spectroscopy of carbonaceous material (RSCM), which is commonly used to estimate the peak metamorphic temperature of rocks, based on quantifying the degree of graphitization of carbonaceous material (CM) during the metamorphism (Beyssac et al., 2002). The method has been recently applied in provenance studies in the Southern Alps of New Zealand (Herman et al., 2015; Nibourel et al., 2015): distributions of the estimated peak metamorphic temperatures from detrital samples were used to infer the erosion patterns of the source areas, assuming that the weathering intensity of CM is low and that there are no systematic biases introduced by denudation, transport and weathering processes. This main assumption, the preservation of CM tracer along the pathway from bedrock outcrops to the deposition, is also adopted in this study, but the caveats of the method and the potential bias associated with the possible weathering of the rock-derived CM are discussed in the Data Repository.

SETTING

The Southern Alps extend along the Alpine Fault, a major transpressional boundary between the Australian and Pacific plates in the South Island of New Zealand. In the western Southern Alps since at least ~6–4 Ma (Sutherland, 1996; Walcott, 1998), rocks have been exhumed from upper to lower crustal levels and are exposed within a narrow, 15–30 km zone, presenting a metamorphic gradient sub-perpendicular to both the mountain strike and the Alpine Fault (Beyssac et al., 2016). In the central part of the range, rapid rock uplift and high precipitation have maintained high erosion rates up to ~6–9 mm/yr over millennium to million-year time scales during the Plio-Pleistocene (Herman et al., 2010; Hovius et al., 1997; Tippett and Kamp, 1993), whereas in the southwest of the range the long-term rock exhumation rate decreases to ~1–2 mm/yr (Jiao et al., 2017; Tippett and Kamp, 1993). At the LGM the Southern Alps were extensively glaciated (Barrell, 2011), but now, in the study area, glacier névés only occur at the highest elevations (Fig. 1). In the areas of principal interest to this study, the Waiatoto and Arawhata catchments (see DISCUSSION), the two dominant rock types are chlorite and biotite schists (Fig. 1), which contain CM that record peak metamorphic temperatures in the ranges of 298–625 °C and 394–641 °C, respectively (single-grain data from Beyssac et al., 2016). Chlorite schist (CS), constituting ~38% of the surface area in the catchments, is distributed mainly in the upper valleys near the Main Divide (>15–20 km horizontal distance to the mountain front), whereas biotite schist (BS), ~48% of the surface area, is more proximal (<15–20 km) to the Alpine Fault and at lower elevations (mostly <1000 m) (Fig. 2). The surface area (~14%) of other schist/semischist (garnet and upper amphibolite and sub-greenschist facies) is significantly smaller than the chlorite and biotite schists. West of the Alpine Fault, the bedrocks comprise metamorphosed sandstones, gneisses and minor granitoids that are covered by glacial gravels (Rattenbury et al., 2010), which are much less eroded than the schists in the Southern Alps and significantly underrepresented in the river bedload (Cox and Nibourel, 2015; Sutherland, 1996).

SAMPLES AND METHODS

Sediment samples (silts and clays) were collected from a piston core (TAN0712–27; −43.753917°, 168.150617°; 1369 m water depth) on the northern levee of the Waiatoto Canyon (Fig. 1). The age model (from ~21 ka to <1 ka) of the core is constrained by three radiocarbon dates and environmental magnetic correlation with a nearby core (Fig. DR2; Tables DR1 and DR2). Twenty-seven samples were collected at every 10 cm, and each is 1 cm long and integrates sedimentation over periods from a few decades to more than one hundred years. X-ray diffraction (XRD) analysis suggests dominance of phyllosilicates, quartz, plagioclase and lesser calcite and K-feldspar (Fig. DR1), consistent with expected mineralogy of a terrestrial-dominated sediment derived from the schist in the Southern Alps. Phyllosilicates include white mica (phengite), chlorite, with lesser vermiculite (perhaps from weathered biotite) and traces of serpentine minerals (Fig. DR1). Eight samples were selected for RSCM analyses, and 185–228 CM particles were measured for each sample (Table DR3). In order to construct RSCM temperature distributions for different metamorphic source rocks in the Southern Alps, we obtained data from 16 bedrock samples from the Waiatoto and Arawhata catchments (Table DR3) and added them to the dataset reported by Beyssac et al. (2016). To address the tracer concentration variation in the bedrocks, we analyzed total carbon from sands collected in the rivers draining to the west coast from the Southern Alps (Table DR4), and compiled existing total organic carbon (TOC) data from the literature (Table DR5). More details regarding the core, age model and analyses (magnetic, XRD, RSCM and TOC) are described in the Data Repository.

RESULTS

RSCM results indicate that the peak metamorphic temperatures of the CM grains in the samples range between 213 and 626 °C, with the majority between 375 and 575 °C (Fig. DR5). By comparing to the bedrock data (Fig. DR4), we estimate an optimized CM composition in terms of their source rocks through a Monte Carlo simulation, and use a ratio of 0.6–1 for the tracer abundance in the chlorite schist (CS) relative to the biotite and amphibolite schists, for accommodating the observed variation in CM concentration in the bedrocks (Data Repository). The results suggest that the majority (>90%) of the CM originate from the chlorite and biotite schists. In the Holocene samples (i.e., ~9.1–0.8 ka), 86–91% of the CM are modelled to be from the CS, and considering the tracer abundance variation in source rocks, the proportion of the bulk CS sediments could be up 91–93% (Fig. 3).

The mixing model applied to the LGM sample (21.2 ka) predicts 65.5% CM from the CS, which corresponds to 65.5–75% bulk sediments using the relative tracer abundance ratio mentioned above, markedly lower than the Holocene samples. During the last deglaciation, the models suggest an increased proportion of the CS-derived CM from 73% at 14.3 ka to 87% at 9.1 ka, corresponding to an increased proportion of the CS sediments from 73–81% to 87–91% (Fig. 3).

DISCUSSION

The narrow continental shelf (~15 km) and poorly sorted bed sediments suggest the submarine canyon is active and mainly fed by high river discharges sourced from high rainfalls, storms or earthquakes. Most of the sediment load is transported to the deep Tasman Sea, and the dominant deposition on the canyon levee comprises turbidity current overspill and hemipelagic sediments with negligible influence from surface ocean currents (Fig. DR6). The narrow coastal plain along the west coast of the South Island facilitates rapid delivery of most of the particulate sediments from the Southern Alps through the fluvial system to offshore. During the last glaciation, the sediment transport to the ocean was probably more efficient, due to rapid glacial evacuation and tidewater termini of glaciers in the region (Barrell, 2011). Therefore, we assume limited impact from the onshore storage on the sediment compositions in the core. The head of the Waiatoto Canyon is connected to the present-day Waiatoto and Arawhata rivers, whose catchments we postulate as the primary provenance for sediments in the core. This is supported by the observation that the quartz content in the core sediments is consistent with that measured in the modern sands from these two catchments, but lower than that from most other rivers draining the western flank of the Southern Alps (Fig. DR3). Some sediments in the core were perhaps also derived from the smaller Turnbull and Okuru, or the bigger Haast-Landsborough catchments, but including them as additional source areas does not materially affect our conclusions (Data Repository).

Sedimentation rates in the core show a general increase from the glaciation (<10 cm/kyr) to the Holocene (mostly >15 cm/kyr) (Fig. 3). This is consistent with the erosion history previously estimated from the bedrocks in the southern part of Southern Alps, where the decadal erosion rate (>5 mm/yr) is significantly higher than the average exhumation rate over the Quaternary (<2 mm/yr) (Jiao et al., 2017).

Our mixing models suggest that chlorite schist (CS) is the major source of the sediments in the offshore core, but the proportion of CS-derived material shows systematic variation through time. This is compared to the spatial distribution of erosion intensity predicted from models of three different surface processes, in order to infer their relative importance in contributing sediments to the drainage system. During the Holocene, erosion has been concentrated in the CS area in the catchment. We estimate the potential distribution of fluvial incision based on the unit stream power, which can be approximated by an upstream drainage area A and a channel slope S ($\varepsilon = A^{0.5}S$, e.g., Finlayson et al., 2002). This calculation predicts high incision rates in the steep tributaries (Fig. DR7), with no significant contrast between the upper and lower valleys. On the other hand, mapped large (affecting area >0.2 km^2) landslides are mainly located >30 km upstream (or >15 km in horizontal distance) from the Alpine Fault (Fig. 2; Fig. DR7) (Heron, 2014). We estimate that the CS sediments produced by landslides makes up ~64% of the total evacuated hillslope materials in the inventory of Heron (2014), using a volume-area scaling exponent of 1.5 (Larsen et al., 2010). Therefore, driven by the rapid rock uplift and relief production, the higher temporal frequency and larger affecting area of slope failures in the upper valleys relative to the low areas, support rock landslides to be the most significant sediment-contributing process during the last 9 ka, although the spatial analysis based on the current inventory does not fully reproduce the estimated very high proportion (86–93%) of CS sediments in the terrestrial component of the Holocene sediments.

The inferred erosion pattern during glaciation is different. A best-fit ice-sheet model for the LGM (Golledge et al., 2012) predicts fast flowing glaciers on the trunk beds of the mountain valleys, with particularly high velocities within 15 km from the Alpine Fault (Fig. DR7). As the rate of glacial abrasion may scale nonlinearly with the basal sliding velocity (Herman et al., 2015; Koppes et al., 2015), the low valleys formed by the biotite zone and amphibolite schist would have been preferentially carved by glaciers. Using the sliding velocity squared μ^2 as a proxy for glacial erosion, the materials produced by glacial abrasion are expected to contain only 29% sediments from the CS. Therefore, compared to the present-day near ice-free condition, erosion during the glaciation would produce a higher proportion of the higher-grade metamorphic rocks; this is consistent with the decreased portion of CS sediments in the deeper samples in the core.

From the LGM to early Holocene, the erosional change in the Southern Alps is synchronous with both global and regional warming of the atmospheric temperature (Fig. 3). During this period, snowlines on the eastern flank of the Southern Alps rose by over 226–360 m in elevation (Fig. 3)(Kaplan et al., 2013; Putnam et al., 2012). Due to higher precipitation rates, the ice mass to the west of the Main Divide is more sensitive to a warming climate and has receded more substantially following the LGM, with an Equilibrium line altitude (ELA) difference estimated over 1000 m (Golledge et al., 2012) (Fig. 2). Therefore, we suggest that the relative increase in erosion contribution from the high CS areas was a consequence of upstream retreat of the glaciers, which decelerated the erosion of the low-lying biotite zone and higher-grade schists. In addition, seasonal fluctuation of the ice mass may trigger increasing failures of steeper slopes in the CS areas near the present ELA (Fig. 2), which is supported by the frequent rock avalanches observed in the current periglacial zones (Allen et al., 2011; Augustinus, 1992). During the Holocene, the sediment composition has been generally constant, in accord with the trends of the global atmospheric temperature and regional snowline elevations, both of which remained relatively steady until the last few hundred years.

ACKOWLEDGMENTS

The crew of RV *Tangaroa* and NIWA TAN0712 cruise participants are gratefully acknowledged. Nick Golledge is thanked for sharing the LGM icefield model. Jiao received scholarships from SERI Switzerland and the Kreitman School. Cox’s contribution was funded by GNS Science’s “Impacts of Global Plate Tectonics in and around New Zealand Programme” (PGST Contract CO5X0203), and Beyssac’s by Sorbonne Université and a PHC Germaine de Stael project (co-PI Adatte). We thank Robert Hilton and the anonymous reviewers for their valuable comments, and Mark Quigley for his editorial handling and advices.

REFERENCES CITED

Allen, S.K., Cox, S.C., and Owens, I.F., 2011, Rock avalanches and other landslides in the central Southern Alps of New Zealand: A regional study considering possible climate change impacts: Landslides, v. 8, p. 33–48, https://doi.org/10.1007/s10346-010-0222-z.

Augustinus, P.C., 1992, The influence of rock mass strength on glacial valley cross-profile morphometry: A case study from the Southern Alps, New Zealand: Earth Surface Processes and Landforms, v. 17, p. 39–51, https://doi.org/10.1002/esp.3290170104.

Barrell, D.J.A., 2011, Quaternary Glaciers of New Zealand, *in* Ehlers, J., Gibbard, P.L., and Philip, D. H., eds., Quaternary Glaciations—Extent and Chronology, Developments in Quaternary Sciences, Volume 15: Amsterdam, Netherlands, Elsevier, p. 1047–1064, https://doi.org/10.1016/B978-0-444-53447-7.00075-1.

Beyssac, O., Cox, S.C., Vry, J., and Herman, F., 2016, Peak metamorphic temperature and thermal history of the Southern Alps (New Zealand): Tectonophysics, v. 676, p. 229–249, https://doi.org/10.1016/j.tecto.2015.12.024.

Beyssac, O., Goffé, B., Chopin, C., and Rouzaud, J.N., 2002, Raman spectra of carbonaceous material in metasediments: A new geothermometer: Journal of Metamorphic Geology, v. 20, p. 859–871, https://doi.org/10.1046/j.1525-1314.2002.00408.x.

Burbank, D.W., Leland, J., Fielding, E., Anderson, R.S., Brozovic, N., Reid, M.R., and Duncan, C., 1996, Bedrock incision, rock uplift and threshold hillslopes in the northwestern Himalayas: Nature, v. 379, p. 505–510, https://doi.org/10.1038/379505a0.

Cox, S.C., and Nibourel, L., 2015, Bedload composition, transport and modification in rivers of Westland, New Zealand, with implications for the distribution of alluvial pounamu (jade): New Zealand Journal of Geology and Geophysics, v. 58, p. 154–175, https://doi.org/10.1080/00288306.2015.1025799.

Dadson, S.J., et al., 2003, Links between erosion, runoff variability and seismicity in the Taiwan orogen: Nature, v. 426, p. 648–651, https://doi.org/10.1038/nature02150.

Finlayson, D.P., Montgomery, D.R., and Hallet, B., 2002, Spatial coincidence of rapid inferred erosion with young metamorphic massifs in the Himalayas: Geology, v. 30, p. 219–222, https://doi.org/10.1130/0091-7613(2002)030<0219:SCORIE>2.0.CO;2.

Golledge, N.R., Mackintosh, A.N., Anderson, B.M., Buckley, K.M., Doughty, A.M., Barrell, D.J.A., Denton, G.H., Vandergoes, M.J., Andersen, B.G., and Schaefer, J.M., 2012, Last Glacial Maximum climate in New Zealand inferred from a modelled Southern Alps icefield: Quaternary Science Reviews, v. 46, p. 30–45, https://doi.org/10.1016/j.quascirev.2012.05.004.

Griffiths, G.A., and Glasby, G.P., 1985, Input of river-derived sediment to the New Zealand continental shelf: I. Mass: Estuarine, Coastal and Shelf Science, v. 21, p. 773–787, https://doi.org/10.1016/0272-7714(85)90072-1.

Hallet, B., Hunter, L., and Bogen, J., 1996, Rates of erosion and sediment evacuation by glaciers: A review of field data and their implications: Global and Planetary Change, v. 12, p. 213–235, https://doi.org/10.1016/0921-8181(95)00021-6.

Herman, F., Beyssac, O., Brughelli, M., Lane, S.N., Leprince, S., Adatte, T., Lin, J.Y.Y., Avouac, J.-P., and Cox, S.C., 2015, Erosion by an Alpine glacier: Science, v. 350, p. 193–195, https://doi.org/10.1126/science.aab2386.

Herman, F., and Champagnac, J.-D., 2016, Plio-Pleistocene Increase in Erosion Rates in Mountain Belts in response to Climate Change: Terra Nova, v. 28, p. 2–10, https://doi.org/10.1111/ter.12186.

Herman, F., Rhodes, E.J., Braun, J., and Heiniger, L., 2010, Uniform erosion rates and relief amplitude during glacial cycles in the Southern Alps of New Zealand, as revealed from OSL-thermochronology: Earth and Planetary Science Letters, v. 297, p. 183–189, https://doi.org/10.1016/j.epsl.2010.06.019.

Herman, F., Seward, D., Valla, P.G., Carter, A., Kohn, B., Willett, S.D., and Ehlers, T.A., 2013, Worldwide acceleration of mountain erosion under a cooling climate: Nature, v. 504, p. 423–426, https://doi.org/10.1038/nature12877.

Heron, D.W., 2014, Geological Map of New Zealand, Institute of Geological and Nuclear Sciences 1:250,000 geological map 1: Lower Hutt, New Zealand, GNS Science, 1 CD.

Hovius, N., Stark, C.P., and Allen, P.A., 1997, Sediment flux from a mountain belt derived by landslide mapping: Geology, v. 25, p. 231–234, https://doi.org/10.1130/0091-7613(1997)025<0231:SFFAMB>2.3.CO;2.

Jiao, R., Herman, F., and Seward, D., 2017, Late Cenozoic exhumation model of New Zealand: Impacts from tectonics and climate: Earth-Science Reviews, v. 166, p. 286–298, https://doi.org/10.1016/j.earscirev.2017.01.003.

Kaplan, M.R., et al., 2013, The anatomy of long-term warming since 15 ka in New Zealand based on net glacier snowline rise: Geology, v. 41, p. 887–890, https://doi.org/10.1130/G34288.1.

Koppes, M., Hallet, B., Rignot, E., Mouginot, J., Wellner, J.S., and Boldt, K., 2015, Observed latitudinal variations in erosion as a function of glacier dynamics: Nature, v. 526, p. 100–103, https://doi.org/10.1038/nature15385.

Koppes, M.N., and Montgomery, D.R., 2009, The relative efficacy of fluvial and glacial erosion over modern to orogenic timescales: Nature Geoscience, v. 2, p. 644–647, https://doi.org/10.1038/ngeo616.

Larsen, I.J., and Montgomery, D.R., 2012, Landslide erosion coupled to tectonics and river incision: Nature Geoscience, v. 5, p. 468–473, https://doi.org/10.1038/ngeo1479.

Larsen, I.J., Montgomery, D.R., and Korup, O., 2010, Landslide erosion controlled by hillslope material: Nature Geoscience, v. 3, p. 247–251, https://doi.org/10.1038/ngeo776.

Neil, H., Mitchell, J., Wilcox, S., Gerring, P., Bostock, H., and Northcote, L., 2007, West Coast Canyons 2 (TAN0712) NIWA voyage report (10 September–4 October 2017): National Institute of Water and Atmospheric Research, Wellington, New Zealand.

Nibourel, L., Herman, F., Cox, S.C., Beyssac, O., and Lavé, J., 2015, Provenance analysis using Raman spectroscopy of carbonaceous material: A case study in the Southern Alps of New Zealand: Journal of Geophysical Research. Earth Surface, v. 120, p. 2056–2079, https://doi.org/10.1002/2015JF003541.

Petit, J.R., et al., 1999, Climate and atmospheric history of the past 420,000 years from the Vostok ice core, Antarctica: Nature, v. 399, p. 429–436, https://doi.org/10.1038/20859.

Putnam, A.E., Schaefer, J.M., Denton, G.H., Barrell, D.J.A., Finkel, R.C., Andersen, B.G., Schwartz, R., Chinn, T.J.H., and Doughty, A.M., 2012, Regional climate control of glaciers in New Zealand and Europe during the pre-industrial Holocene: Nature Geoscience, v. 5, p. 627–630, https://doi.org/10.1038/ngeo1548.

Rattenbury, M.S., Jongens, R., and Cox, S.C., 2010, Geology of the Haast area. Institute of Geological and Nuclear Sciences 1:250,000 geological map 14: Lower Hutt, New Zealand, GNS Science, 58 p. + 1 folded map.

Sutherland, R., 1996, Transpressional development of the Australia-Pacific boundary through southern South Island, New Zealand: Constraints from Miocene-Pliocene sediments, Waiho-1 borehole, South Westland: New Zealand Journal of Geology and Geophysics, v. 39, p. 251–264, https://doi.org/10.1080/00288306.1996.9514709.

Tippett, J.M., and Kamp, P.J.J., 1993, Fission Track Analysis of the Late Cenozoic Vertical Kinematics of Continental Pacific Crust, South Island, New Zealand: Journal of Geophysical Research, v. 98, p. 16119–16148, https://doi.org/10.1029/92JB02115.

Walcott, R.I., 1998, Modes of oblique compression: Late Cenozoic tectonics of the South Island of New Zealand: Reviews of Geophysics, v. 36, p. 1–26, https://doi.org/10.1029/97RG03084.

Willenbring, J.K., and Jerolmack, D.J., 2016, The null hypothesis: globally steady rates of erosion, weathering fluxes and shelf sediment accumulation during Late Cenozoic mountain uplift and glaciation: Terra Nova, v. 28, p. 11–18, https://doi.org/10.1111/ter.12185.

Williams, P.W., King, D.N.T., Zhao, J.X., and Collerson, K.D., 2005, Late Pleistocene to Holocene composite speleothem 18O and 13C chronologies from South Island, New Zealand—Did a global Younger Dryas really exist?: Earth and Planetary Science Letters, v. 230, p. 301–317, https://doi.org/10.1016/j.epsl.2004.10.024.

Willsman, A.P., Chinn, T., Hendrikx, J., and Lorrey, A., 2010, New Zealand glacier monitoring: End of summer snowline survey 2010: Auckland, New Zealand, National Institute of Water and Atmospheric Research, 146 p.

Zhang, P., Molnar, P., and Downs, W.R., 2001, Increased sedimentation rates and grain sizes 2–4 Myr ago due to the influence of climate change on erosion rates: Nature, v. 410, p. 599–604, https://doi.org/10.1038/35069099.

FIGURE CAPTIONS

Figure 1. Map of the Arawhata and Waiatoto (also Turnbull, Okuru and Haast) catchments in the Southern Alps of New Zealand and the offshore location of the TAN0712-27 core site. Bedrock metamorphism is from Rattenbury et al. (2010) and the bathymetry is from Neil et al. (2007). LGM ice extent is after Barrell (2011). Inset indicates the location of the map area.

Figure 2. River profiles from the Waiatoto and Arawhata catchments. Equilibrium line altitude (ELA) during the Last Glacial Maximum (LGM) is extracted from the best-fit icefield model of Golledge et al. (2012), in comparison to the modern ELA of the Findlay Glacier (Fig. 1) (Willsman et al., 2010). Location and magnitude of landslides are from the inventory of Heron (2014). Proportions of chlorite schist (CS) area out of the total surface area as functions of elevation and upstream distance are plotted along the right and top axes, respectively.

Figure 3. Sedimentary records compared to climate and snowline histories. Climate records are from the Vostok ice core, Antarctica (Petit et al., 1999) and New Zealand speleothem (Williams et al., 2005). Snowline elevation changes are from the Whale

Stream (west branch) glacier (Kaplan et al., 2013) and the Cameron and Mt. Cook glaciers (Putnam et al., 2012). Sedimentation rates are estimated from the age model using spline (solid) and linear (dashed) interpolations. Sediment provenance is indicated as the estimated proportion of chlorite schist (CS) sediments, assuming a relative tracer abundance of 0.8±0.2 (line and envelope); error bar indicates a combined uncertainty from tracer abundance and standard deviation of the sediment mixing models.

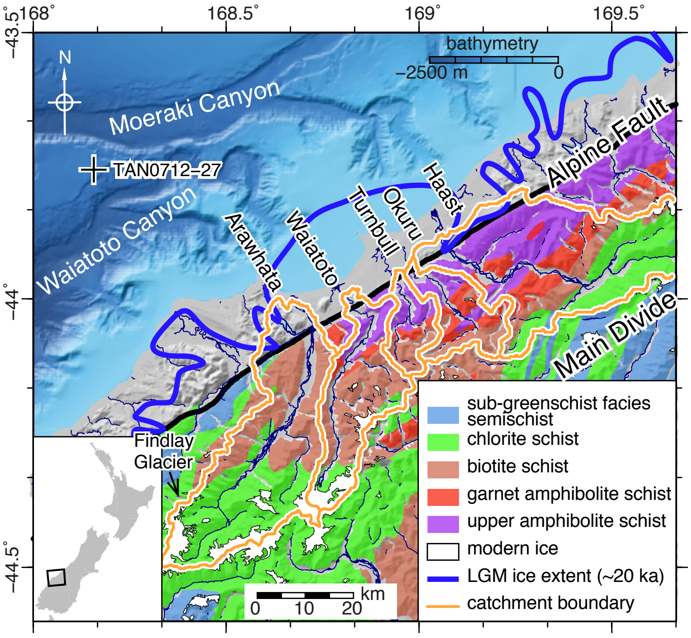

168°
168.5°
169°
169.5°
−43.5°
−44°
−44.5°
bathymetry
−2500 m
0
N
Moeraki Canyon
TAN0712-27
Waiatoto Canyon
Arawhata
Waiatoto
Turnbull
Okuru
Haast
Alpine Fault
Main Divide
Findlay Glacier
sub-greenschist facies semischist
chlorite schist
biotite schist
garnet amphibolite schist
upper amphibolite schist
modern ice
LGM ice extent (~20 ka)
catchment boundary
km
0
10
20

Figure 1

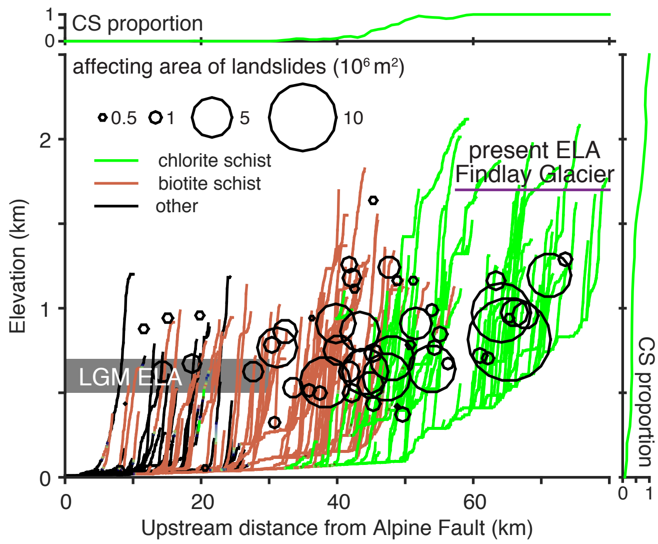
CS proportion
affecting area of landslides (10^6 m^2)
0.5
1
5
10
chlorite schist
biotite schist
other
present ELA
Findlay Glacier
LGM ELA
Elevation (km)
Upstream distance from Alpine Fault (km)
CS proportion
0
1
2
20
40
60

Figure 2

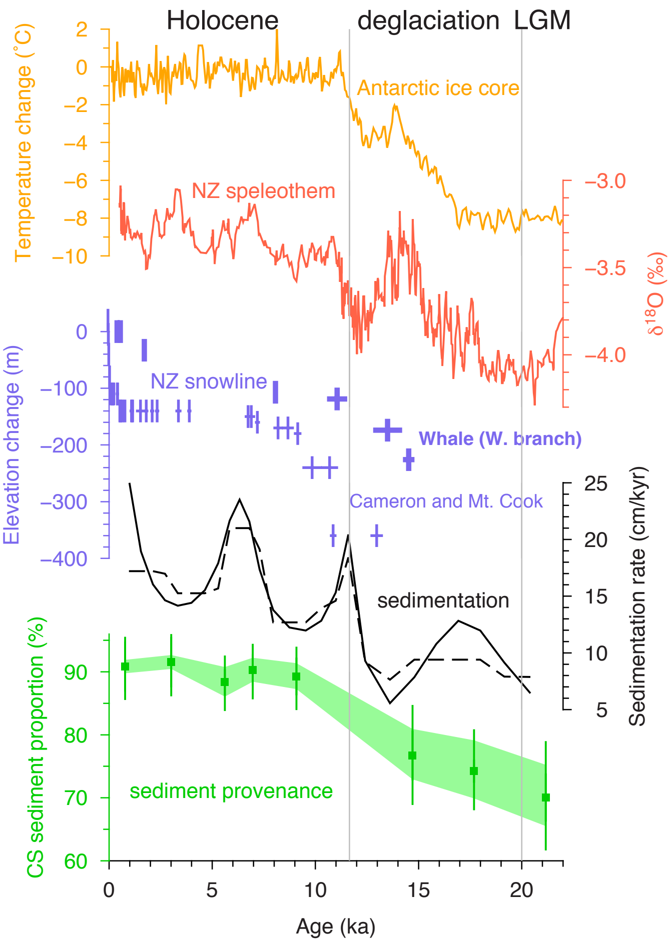

Holocene
deglaciation
LGM
Antarctic ice core
NZ speleothem
NZ snowline
Whale (W. branch)
Cameron and Mt. Cook
sedimentation
sediment provenance
Temperature change (°C)
δ18O (‰)
Elevation change (m)
Sedimentation rate (cm/kyr)
CS sediment proportion (%)
Age (ka)
2
0
−2
−4
−6
−8
−10
−3.0
−3.5
−4.0
0
−100
−200
−300
−400
25
20
15
10
5
90
80
70
60
0
5
10
15
20

Figure 3

Figure DR1

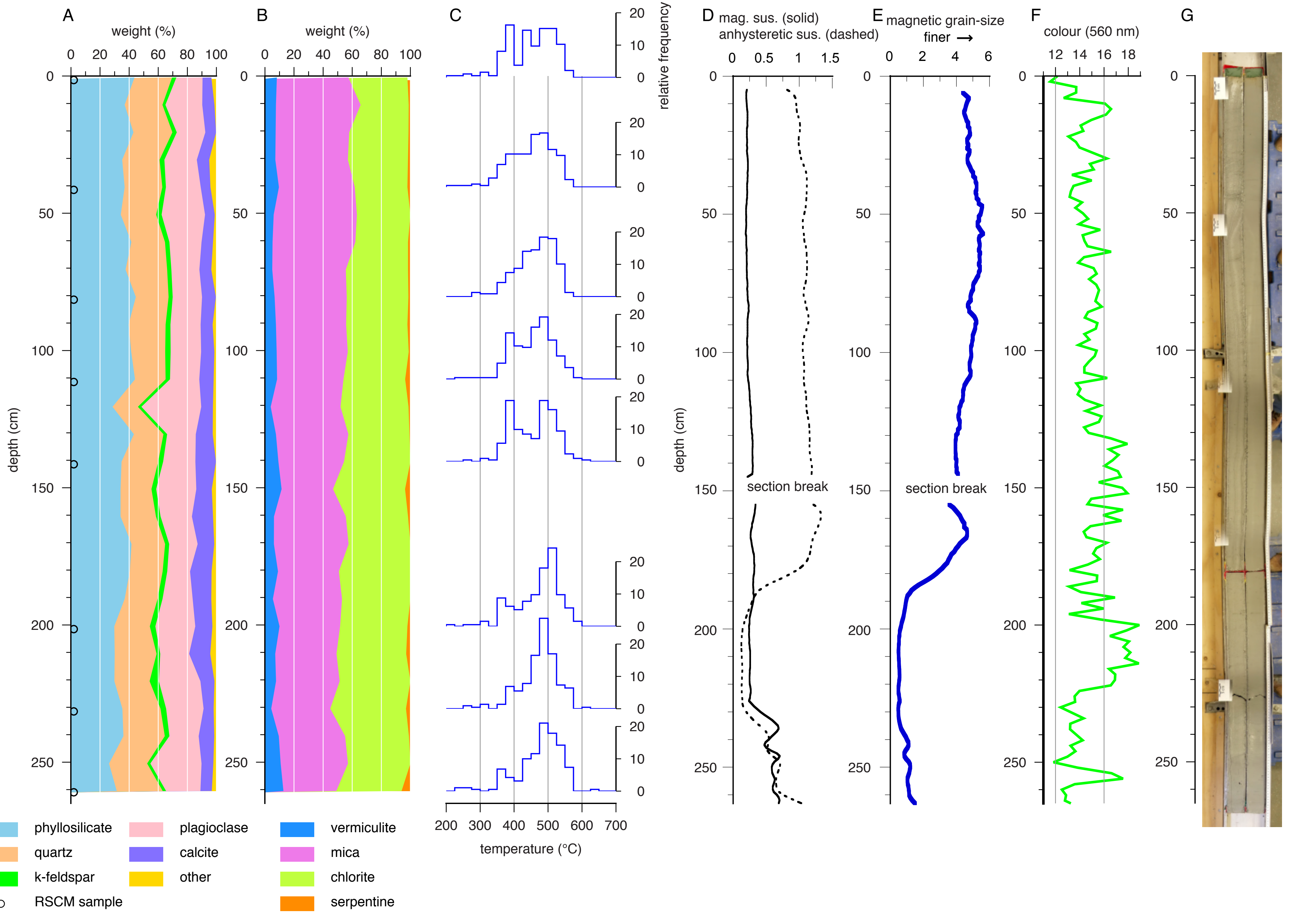
A
weight (%)
0 20 40 60 80 100
depth (cm)
0 50 100 150 200 250
B
weight (%)
0 20 40 60 80 100
C
relative frequency (%)
0 10 20
200 300 400 500 600 700
temperature (°C)
D mag. sus. (solid)
anhysteretic sus. (dashed)
0 0.5 1 1.5
section break
E magnetic grain-size
finer ⟶
0 2 4 6
section break
F
colour (560 nm)
12 14 16 18
G
phyllosilicate
quartz
k-feldspar
RSCM sample
plagioclase
calcite
other
vermiculite
mica
chlorite
serpentine

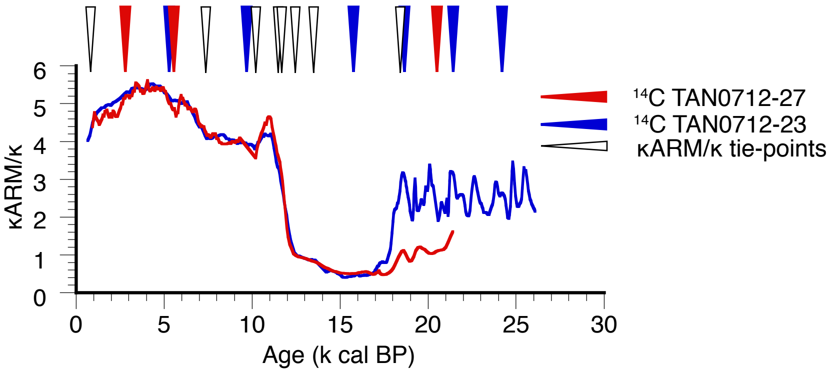

6
5
4
3
2
1
0
κARM/κ
0
5
10
15
20
25
30
Age (k cal BP)
14C TAN0712-27
14C TAN0712-23
κARM/κ tie-points

Figure DR2

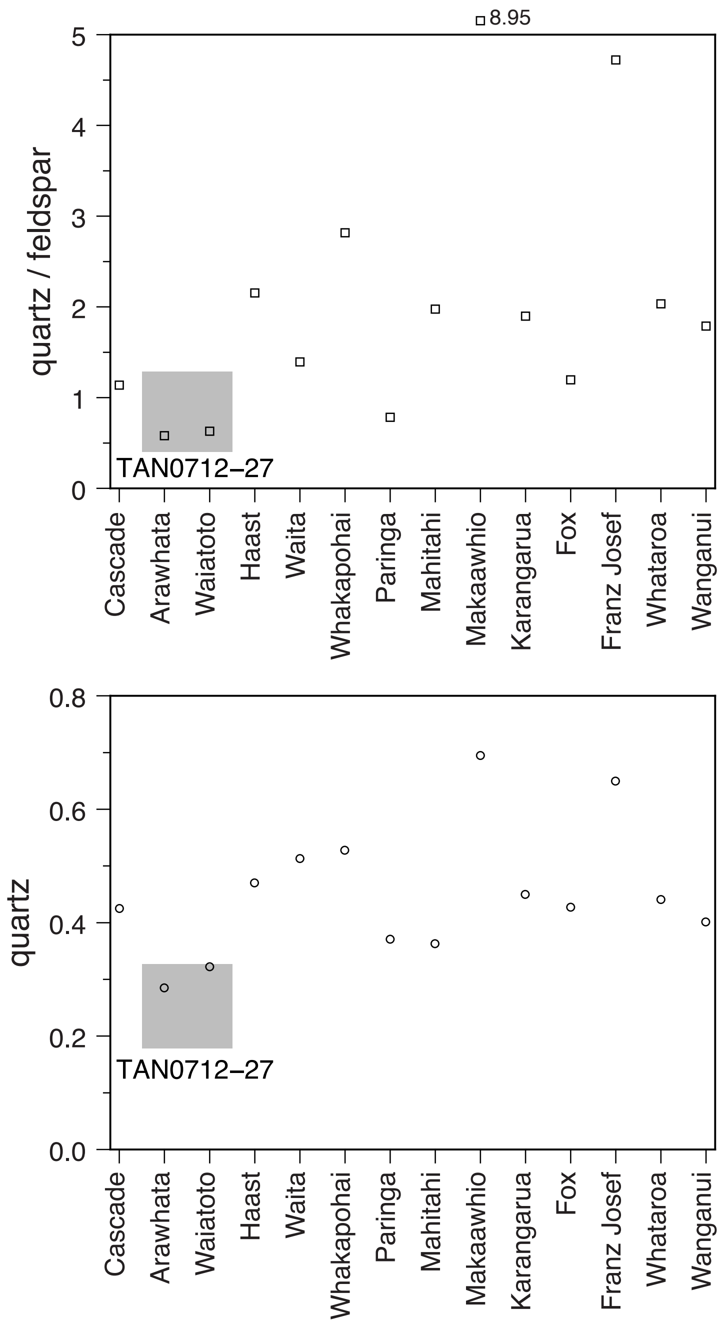

8.95
5
4
3
2
1
0
quartz / feldspar
TAN0712–27
Cascade
Arawhata
Waiatoto
Haast
Waita
Whakapohai
Paringa
Mahitahi
Makaawhio
Karangarua
Fox
Franz Josef
Whataroa
Wanganui
0.8
0.6
0.4
0.2
0.0
quartz
TAN0712–27
Cascade
Arawhata
Waiatoto
Haast
Waita
Whakapohai
Paringa
Mahitahi
Makaawhio
Karangarua
Fox
Franz Josef
Whataroa
Wanganui

Figure DR3

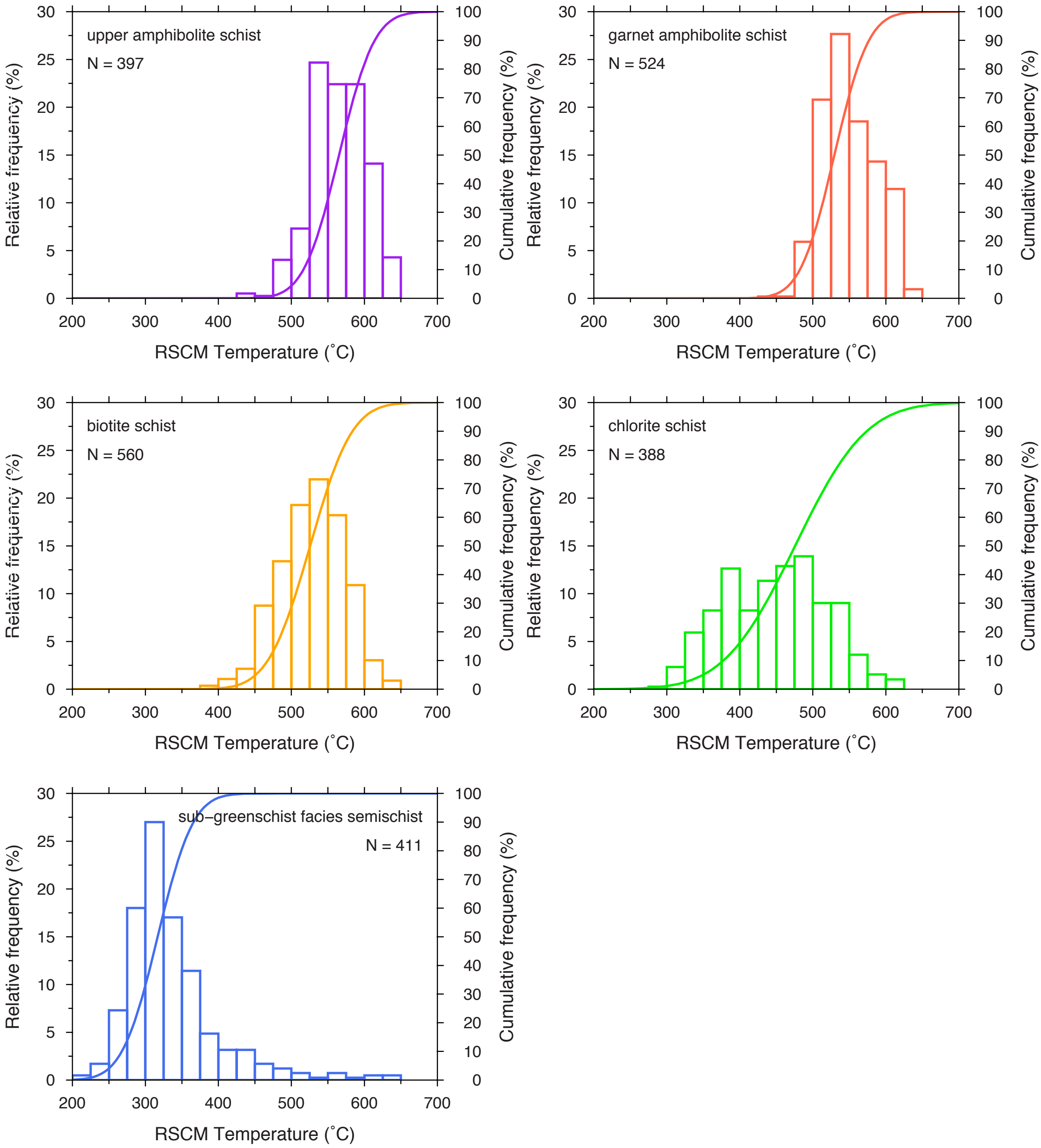
upper amphibolite schist
N = 397
garnet amphibolite schist
N = 524
biotite schist
N = 560
chlorite schist
N = 388
sub−greenschist facies semischist
N = 411
Relative frequency (%)
Cumulative frequency (%)
RSCM Temperature (˚C)

Figure DR4

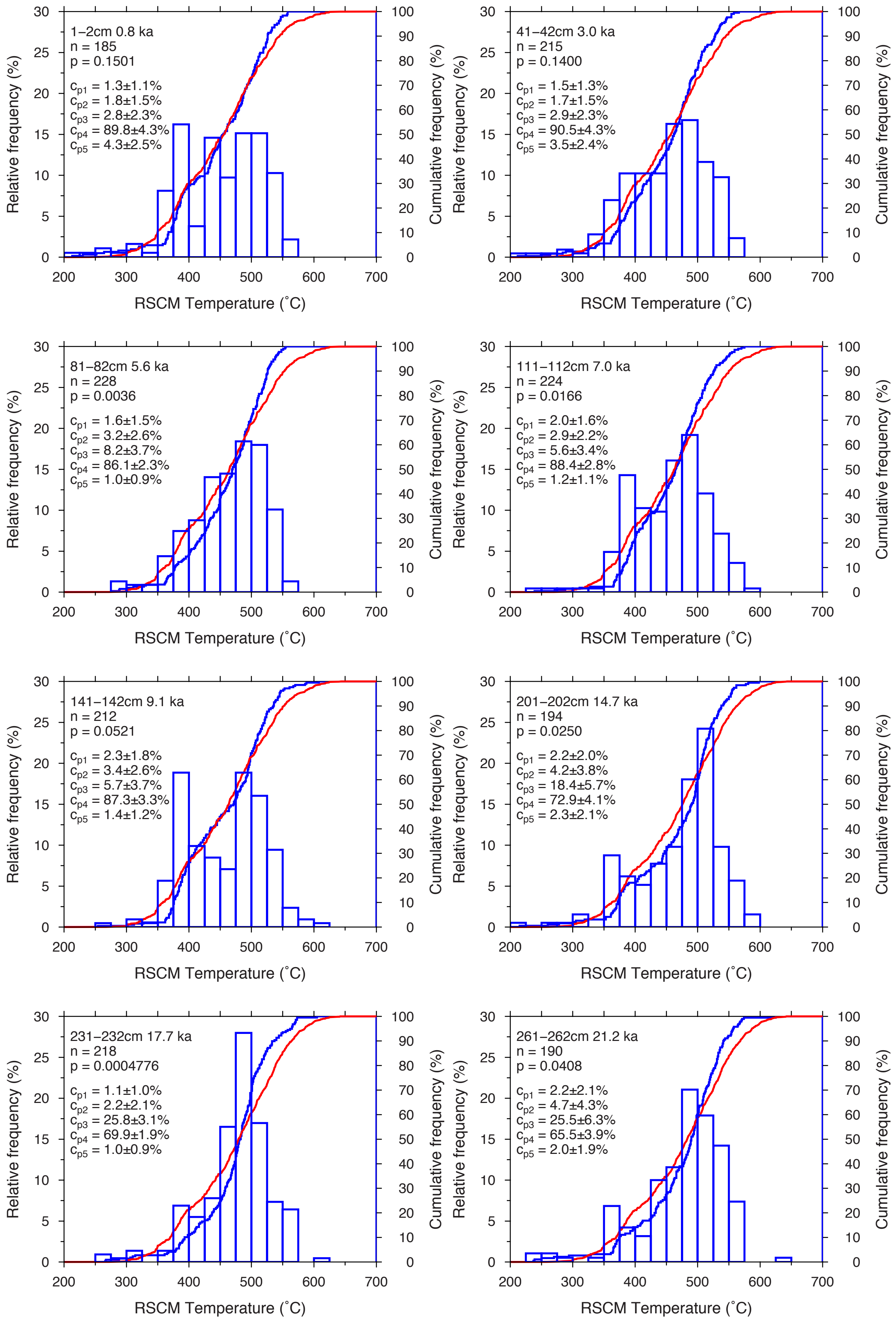

1–2cm 0.8 ka
n = 185
p = 0.1501
c_{p1} = 1.3±1.1%
c_{p2} = 1.8±1.5%
c_{p3} = 2.8±2.3%
c_{p4} = 89.8±4.3%
c_{p5} = 4.3±2.5%
41–42cm 3.0 ka
n = 215
p = 0.1400
c_{p1} = 1.5±1.3%
c_{p2} = 1.7±1.5%
c_{p3} = 2.9±2.3%
c_{p4} = 90.5±4.3%
c_{p5} = 3.5±2.4%
81–82cm 5.6 ka
n = 228
p = 0.0036
c_{p1} = 1.6±1.5%
c_{p2} = 3.2±2.6%
c_{p3} = 8.2±3.7%
c_{p4} = 86.1±2.3%
c_{p5} = 1.0±0.9%
111–112cm 7.0 ka
n = 224
p = 0.0166
c_{p1} = 2.0±1.6%
c_{p2} = 2.9±2.2%
c_{p3} = 5.6±3.4%
c_{p4} = 88.4±2.8%
c_{p5} = 1.2±1.1%
141–142cm 9.1 ka
n = 212
p = 0.0521
c_{p1} = 2.3±1.8%
c_{p2} = 3.4±2.6%
c_{p3} = 5.7±3.7%
c_{p4} = 87.3±3.3%
c_{p5} = 1.4±1.2%
201–202cm 14.7 ka
n = 194
p = 0.0250
c_{p1} = 2.2±2.0%
c_{p2} = 4.2±3.8%
c_{p3} = 18.4±5.7%
c_{p4} = 72.9±4.1%
c_{p5} = 2.3±2.1%
231–232cm 17.7 ka
n = 218
p = 0.0004776
c_{p1} = 1.1±1.0%
c_{p2} = 2.2±2.1%
c_{p3} = 25.8±3.1%
c_{p4} = 69.9±1.9%
c_{p5} = 1.0±0.9%
261–262cm 21.2 ka
n = 190
p = 0.0408
c_{p1} = 2.2±2.1%
c_{p2} = 4.7±4.3%
c_{p3} = 25.5±6.3%
c_{p4} = 65.5±3.9%
c_{p5} = 2.0±1.9%
Relative frequency (%)
Cumulative frequency (%)
RSCM Temperature (˚C)

Figure DR5

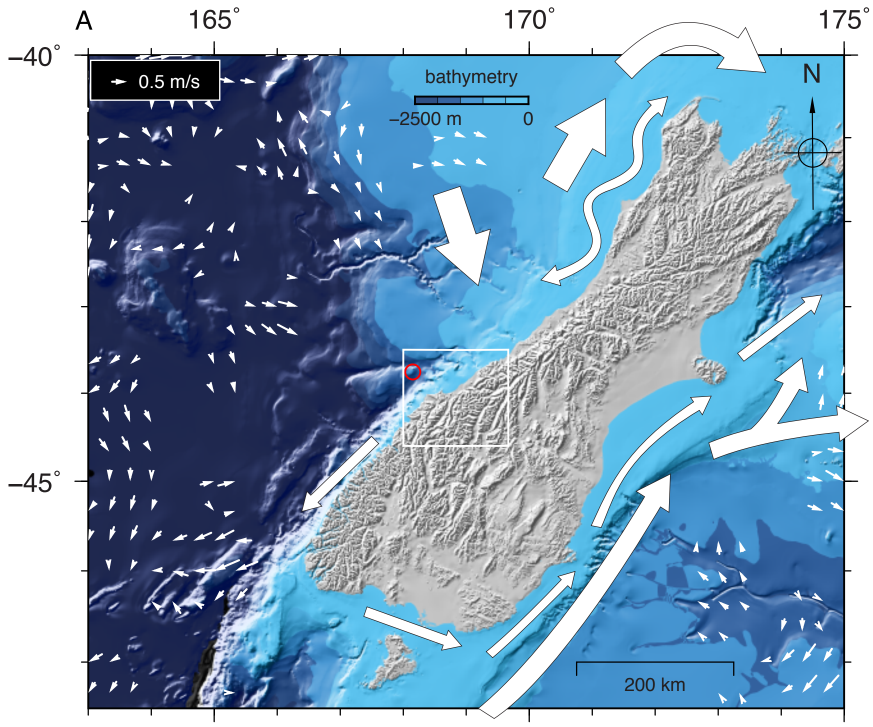

Figure DR6

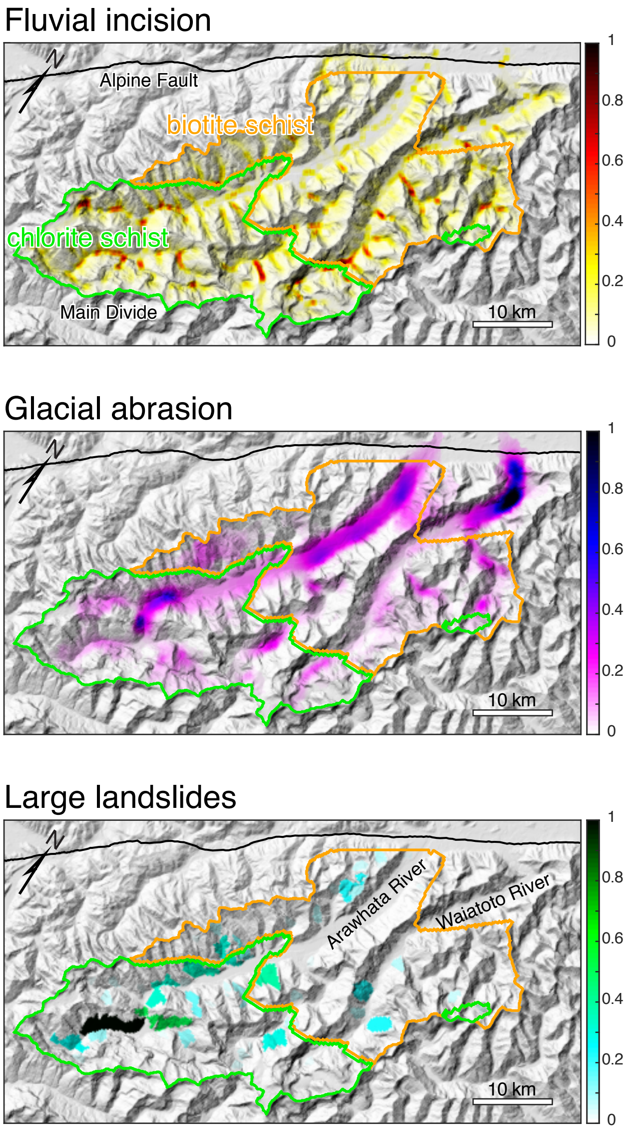
Fluvial incision
Alpine Fault
biotite schist
chlorite schist
Main Divide
10 km
1
0.8
0.6
0.4
0.2
0
Glacial abrasion
10 km
1
0.8
0.6
0.4
0.2
0
Large landslides
Arawhata River
Waiatoto River
10 km
1
0.8
0.6
0.4
0.2
0

Figure DR7

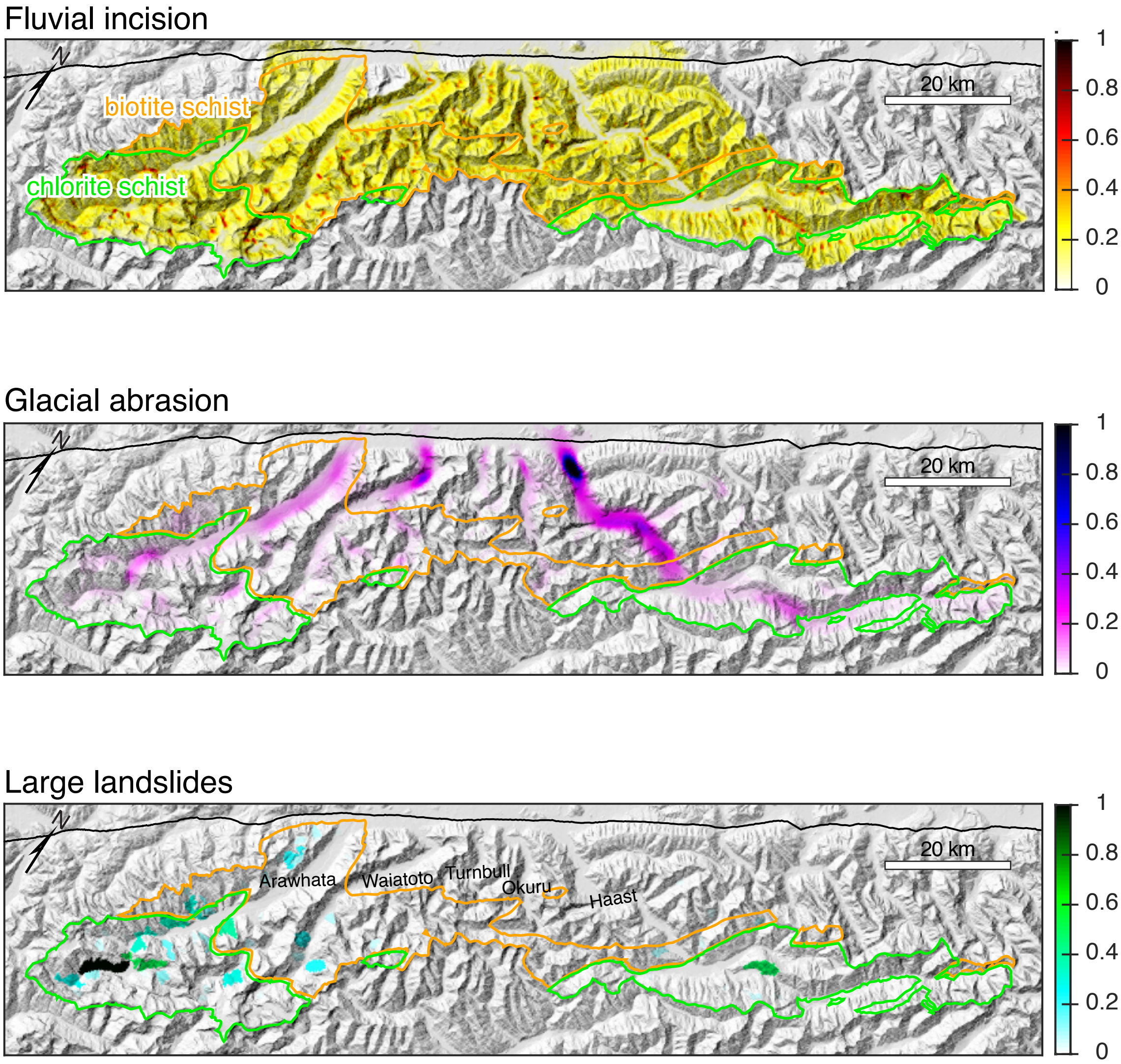
Fluvial incision
biotite schist
chlorite schist
20 km
1
0.8
0.6
0.4
0.2
0
Glacial abrasion
20 km
1
0.8
0.6
0.4
0.2
0
Large landslides
Arawhata
Waiatoto
Turnbull
Okuru
Haast
20 km
1
0.8
0.6
0.4
0.2
0

Figure DR8